IOP Publishing Journal of Micromechanics and Microengineering
J. Micromech. Microeng. **27** (2017) 075007 (13pp) https://doi.org/10.1088/1361-6439/aa71d5

Surface patterning of Zr-based metallic glass by laser irradiation induced selective thermoplastic extrusion in nitrogen gas

Hu Huang[1] **and Jiwang Yan**

Faculty of Science and Technology, Department of Mechanical Engineering, Keio University, Yokohama 223-8522, Japan

E-mail: huanghuzy@163.com (H Huang) and yan@mech.keio.ac.jp (J Yan)

Received 24 March 2017, revised 7 May 2017
Accepted for publication 9 May 2017
Published 5 June 2017

Abstract

Hierarchical surface structures on metallic glass (MG) are useful for enhancing the material's functions. In this paper, surface patterning of Zr-based MG was realized by nanosecond pulsed laser irradiation in nitrogen gas. Experimental results showed that three kinds of surface structures, namely, micro grooves, cross-shaped protrusions, and nanoparticles, were generated on the MG surface under specific laser scanning speeds and various laser power intensities and pulse overlap rates. In particular, the formation of cross-shaped protrusions has never been reported in the literature before. The formation mechanism for each kind of surface structure was investigated. In a nitrogen gas environment, cracks are easily generated and the cracked regions have higher laser absorption and localized thermal resistivity than those of the bulk material. Accordingly, the cross-shaped protrusions were ascribed to the selective thermoplastic extrusion of MG material out of the cracks and the laser pulse tracks formed by the preceding laser scans. It was found that the hierarchical surface structures significantly improved the surface hydrophobicity.

Keywords: metallic glass, hierarchical micro structure, laser irradiation, nitrogen gas, crack, hydrophobicity

(Some figures may appear in colour only in the online journal)

1. Introduction

Metallic glasses (MGs) with unique mechanical, physical, and chemical properties [1, 2] are regarded as very promising engineering materials, attracting increasing attention from both scientific and industrial communities [3–7]. To enhance their functions as biomaterials, catalysts, hydrophobic/superhydrophobic materials, surface patterning of MGs is helpful [3, 8–11]. For example, Au- and Ti-based MGs with a nano-scale granular structure prepared by magnetron sputtering exhibited remarkably enhanced catalytic activity [12] and significantly improved biocompatibility [8] because of their high surface areas. Zr–Pd MG thin films with a nano-scale surface structure showed good biocompatibility for potential applications in biochemistry and implant engineering [13]. MG surfaces with hierarchical micro/nano-structures fabricated by thermoplastic forming [9–11, 14] in the supercooled liquid region (SCLR) between the glass transition temperature and the crystallization temperature and those by chemical methods [15, 16] exhibited superhydrophobicity.

Although the aforementioned methods can pattern MG surfaces, some shortcomings exist. Magnetron sputtering method is only suitable for certain kinds of MGs and is not economic when producing large-area micro/nano-structures [17, 18]. Thermoplastic forming method requires expensive moulds. Chemical methods are not environmentally friendly. Thus, new methods for patterning MG surfaces are in urgent need.

It has been reported [19–22] that with a single shot, nanosecond pulsed laser irradiation could induce surface ripples as well as porous structure with 100 nm-scale voids on the MG

[1] Author to whom any correspondence should be addressed.

surface. Furthermore, by nanosecond pulsed laser irradiation in vacuum [23], two layers of micro-/nano-structures could be fabricated on Zr-based MG substrate, laser pulse tracks covered by a cotton-like MG thin film. In our recent research [24], we revealed that when nanosecond pulsed laser irradiation of Zr-based MG was performed in nitrogen gas environment, cracks could be generated in the irradiated region.

Commonly, crack is regarded as a kind of defect that affects the performances and service life of a product. However, when a crack is irradiated by a laser beam, it exhibits some unique physical and electrical characteristics, i.e. enhanced laser absorption and higher localized thermal resistivity [25–29] compared to the surrounding surface region. According to these characteristics, laser irradiation in combination with infrared thermography has been used to detect cracks [25, 27, 28]. For Zr-based MG, cracks can be effectively generated by nanosecond pulsed laser irradiation in nitrogen gas [24]. If the laser irradiation condition is suitably controlled to make the temperature of MG material around cracks over the glass transition point while the temperature of the surrounding surface region below the glass transition point, the MG material around the cracks might undergo local thermal expansion and deformation because of their superplastic flow characteristics [3, 30, 31]. This effect might be able to generate unique micro-/nano-structures on the MG surface.

In this study, patterning of Zr-based MG was performed by nanosecond pulsed laser irradiation in nitrogen gas. By utilizing the laser irradiation induced local deformation and selective thermoplastic extrusion of MG material near the cracks and laser pulse tracks, novel hierarchical micro-/nano-structure generation was attempted on Zr-based MG.

2. Materials and experiments

As-cast $Zr_{41.2}Ti_{13.8}Cu_{12.5}Ni_{10}Be_{22.5}$ (commonly called Vitreloy 1) MG rod with a diameter of 10 mm was cut into slices with a thickness of 1 mm by wire electrical discharge machining (wire-EDM). To remove the crystallization layer formed during wire-EDM [32], mechanical grinding and polishing were performed on these slices using 400, 800, and 1500 grit sand papers in sequence. Laser irradiation was performed on a Nd:YAG nanosecond pulsed laser system (LR-SHG, MegaOpto Co., Ltd, Japan) with a wavelength of 532 nm, a pulse width of 15.4 ns, a laser beam diameter of ~85 μm, and a pulse frequency of 1 kHz. Nitrogen gas with a pressure of 0.05 MPa was used. Various average laser powers, 0.148, 0.382, and 0.595 W corresponding to various peak laser power intensities, 1.3×10^{12}, 3.4×10^{12}, and 5.3×10^{12} W m^{-2}, were implemented for comparison. Furthermore, various scanning speeds, 1, 5, and 10 mm s^{-1} were used. The pulse overlap width between two adjacent scanning lines was set to be 70, 55, 40, and 25 μm for comparison, resulting in the pulse overlap rate r of 82%, 65%, 47%, and 29%, respectively. The aforementioned experimental conditions are summarized in table 1.

After laser irradiation, surface structures of the irradiated regions were detected by a digital microscope (VHX-1000, Keyence, Japan), a color three dimensional (3D) laser scanning microscope (VK-9700, Keyence, Japan), a field emission scanning electron microscope (FE-SEM) (JSM-7600F, JEOL, Japan), an environmental scanning electron microscope (ESEM) (Inspect S50, FEI, USA), and an atomic force microscope (AFM) (AFM 5100N, Hitachi, Japan). The amorphous characteristic of the MG before and after laser irradiation was characterized by an x-ray diffractometer (XRD, D8 Discover, Bruker, Germany). An energy dispersive x-ray spectroscopy (EDX, XFlash Detector 4010, Bruker, Germany) was used to map the element distribution in the laser irradiated region. To observe the subsurface affecting region induced by laser irradiation, the irradiated samples were cut by a low speed diamond saw. The cross-sections were ground and polished, and then etched for 2 min by HNO_3 (6 mol l^{-1}) solution. After cleaning by acetone, the cross-sections were observed by SEM. A contact angle meter (SImage Entry 5, Excimer Inc., Japan) was used to evaluate the hydrophobicity of the as-cast MG surface as well as laser patterned surfaces.

Table 1. Experimental conditions.

Sample material	$Zr_{41.2}Ti_{13.8}Cu_{12.5}Ni_{10}Be_{22.5}$
Laser wavelength (nm)	532
Laser pulse width (ns)	15.4
Laser pulse frequency (kHz)	1
Atmosphere	Nitrogen gas (0.05 MPa)
Peak laser power intensity ($\times 10^{12}$ W m^{-2})	1.3, 3.4, 5.3
Laser scanning speed (mm s^{-1})	1, 5, 10
Pulse overlap rate between two adjacent scanning line r	82%, 65%, 47%, 29%

3. Results and discussion

3.1. Crack formation

Figure 1(a) presents the representative optical morphology of laser irradiated MG surface obtained under a peak laser power intensity of 1.3×10^{12} W m^{-2}, a scanning speed of 1 mm s^{-1}, and a pulse overlap rate r of 47%. Many laser scanning lines are observed, starting from the left and ending at the right. Figures 1(b)–(d) are local enlarged views corresponding to regions 1–3 in figure 1(a) respectively, showing the micro-features of the last scanning line in detail. As shown in region 1 (figure 1(b)) and 3 (figure 1(d)), many crack-like microstructures are radially distributed around a single laser shot. The high resolution SEM morphology in figure 1(e) confirms that the crack-like microstructures are open cracks with nanoparticles covered on the surrounding irradiated surface. Our previous research [24] indicated that these cracks resulted from the formation of ZrN during laser irradiation in nitrogen gas, which increased the thermal mismatch between the re-solidification layer and the MG substrate.

In figure 1(c), line-like microstructures appear in the center of the single scanning line. Combined the morphologies in figures 1(b)–(d), it is noted that line-like microstructures were originated from the open cracks, and thus they are also cracks.

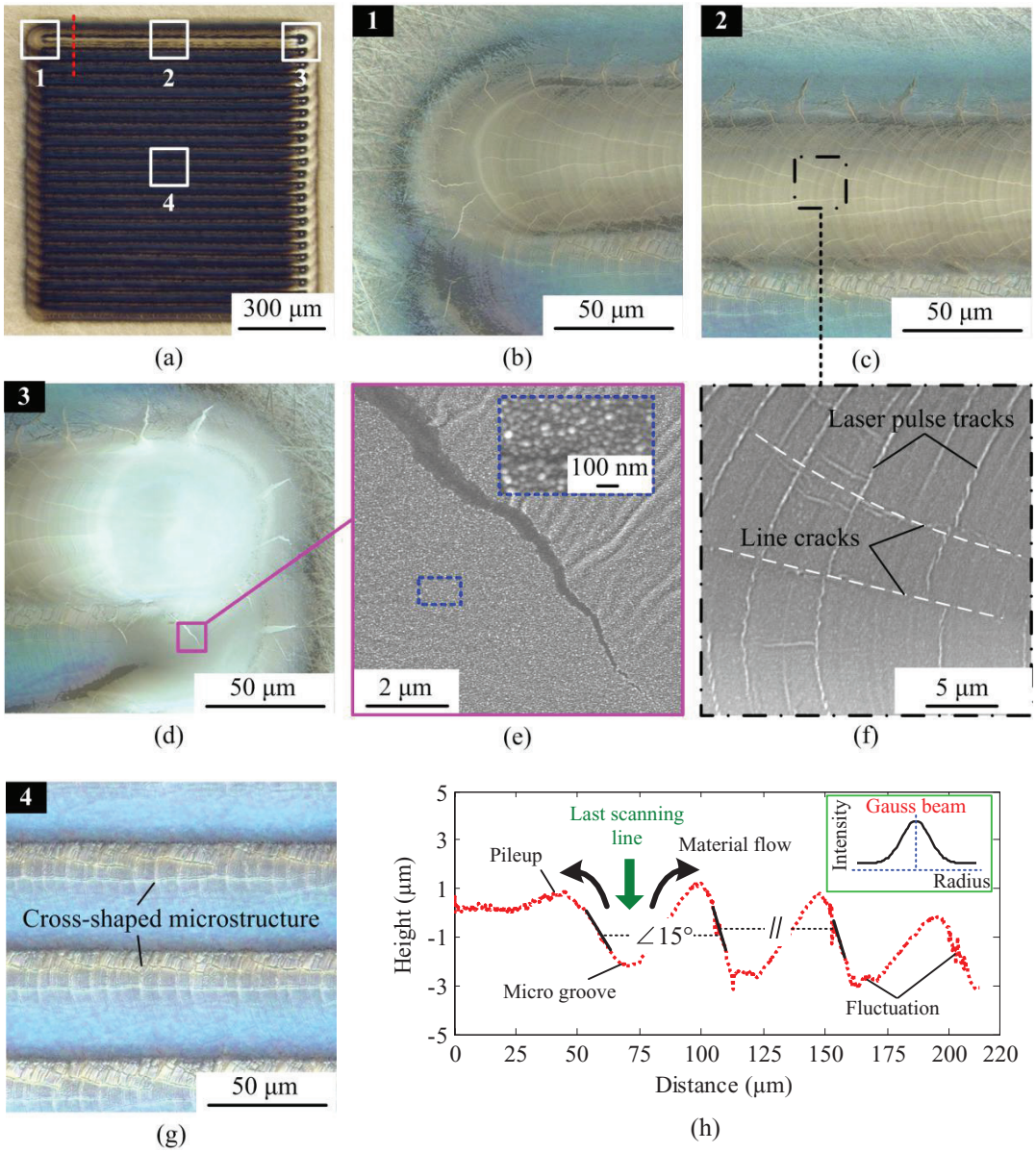

Figure 1. (a) Optical morphology of the irradiated MG surface under a peak laser power intensity of 1.3×10^{12} W m^{-2}, a scanning speed of 1 mm s^{-1}, and a pulse overlap rate r of 47%. (b)–(d) Local micro-features of regions 1–3 at a higher magnification, where crack-like microstructures appear around a single laser shot and line-like microstructures appear in the center of the last laser scanning line. (e) and (f) SEM morphologies showing the crack-like and line-like microstructures in detail. (g) Local micro-features of region 4. (h) Profile of the dotted line in figure 1(a), i.e. the profile of the last three scanning lines. The inserted figure illustrates the intensity of Gauss beam changing with the radius.

However, being different from those surrounding open cracks, these line cracks had evolved to be closed cracks as shown in figure 1(f) (white dashed line) with the role of heating, cooling, and recoil pressure during subsequent laser irradiation along a scanning line. Furthermore, these line cracks were interlaced with the laser pulse tracks formed in the interface between two adjacent laser shots.

Figure 1(g) presents the optical morphology in the center of the irradiated surface, i.e. region 4, where some bright cross-shaped microstructures appear between two laser scanning lines. Due to the resolution limitation of optical microscopes, the cross-shaped microstructures will be further explored in the following sections by SEM.

Figure 1(h) illustrates the profile of the dotted line in figure 1(a), i.e. the profile of the last three scanning lines. Compared to the initial flat surface, both micro groove and pileup were formed on the irradiated surface. The inserted figure illustrates the intensity of Gauss beam changing with the radius. Nanosecond pulsed laser energy was focused on a small irradiation region, causing very fast temperature rise of MG materials. As the laser power intensity changes with the beam radius, the temperature of a single laser shot exhibits a gradient distribution from the center to the outside. In the center of a single laser shot, some MG materials were vaporized as very fine vapor particles because of very high laser power intensity, while near the

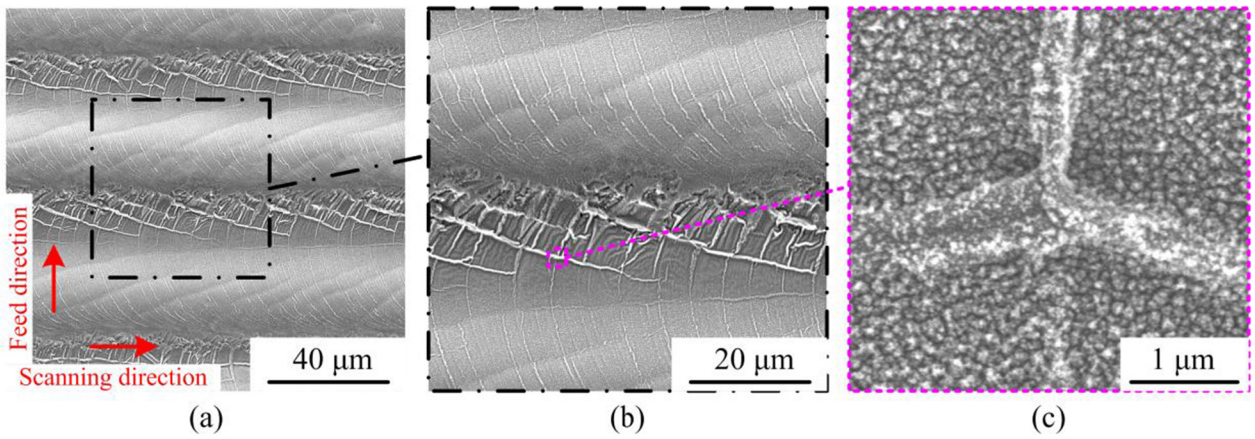

Figure 2. (a) SEM morphology of the irradiated MG surface in region 4, (b) local enlarged view of (a), and (c) local enlarged view of (b).

edge, MG materials may be only liquidized. In the outside, some MG materials were heated in the heat affected zone (HAZ). The recoil pressure generated by vaporization [33] pushed the liquidized and some heated MG materials to flow outward, forming the pileup and micro groove via subsequent re-solidification. The vaporized MG particles were re-deposited and re-solidified on the surface of adjacent laser scanning lines, forming the nanoparticles as shown in figure 1(e). The shape of a single micro groove corresponds to the intensity distribution of laser beam along the radius. When the laser beam scanned along a line, laser pulse tracks were formed in the interface between two adjacent laser shots as shown in figure 1(f).

In figure 1(h), it is also noted that the profile of the last scanning line is almost symmetrical except that the pileup on the right side is slightly higher than that on the left side. On the left side, materials could freely flow on the initially flat surface, while on the right side, previously formed pileup increased the material flow resistance, leading to upward flow of materials and thus higher pileup. In addition, the left sides of profiles in preceding scanning lines are approximatively parallel to each other, but they have an angle of ~15° to that in the last scanning line. This is due to the micro grooves formed by preceding scanning lines that result in the overall deformation of MG materials near the side of preceding scanning lines under the role of recoil pressure generated during the next line scanning. Furthermore, the profile of the last scanning line is smooth, while for the profiles of preceding scanning lines, fluctuation appears on the left side and bottom of micro grooves. This resulted from the cross-shaped microstructures formed during laser interaction between two adjacent scanning lines as shown in figure 1(g).

3.2. Hierarchical surface structures

To show the micro-features of the cross-shaped microstructures in figure 1(g) in detail, figure 2 presents the SEM morphologies of the irradiated MG surface in region 4 at different magnifications. In figure 2(a), periodically cross-shaped microstructures are observed between two laser scanning lines, and their formation positions are much closer to the side of micro groove that near the next scanning line. In figures 2(b) and (c), some MG materials are protruded on the micro groove surface at the positions of line cracks and laser pulse tracks, demonstrating that the formation of cross-shaped protrusions is related to both the line cracks and laser pulse tracks. Furthermore, in figure 2(c), cross-shaped protrusions as well as surrounding surface are covered by nanoparticles, which were generated by re-deposition of the vaporized materials [23]. Accordingly, three kinds of surface structures, namely, micro grooves, cross-shaped protrusions and nanoparticles, have been formed on Zr-based MG surface by nanosecond pulse laser irradiation in nitrogen gas.

3.3. Effects of laser irradiation conditions

To study the effects of laser irradiation conditions on the formation of surface structures, laser irradiations were performed on the Zr-based MG surface under various scanning speeds, laser power intensities, and pulse overlap rates. After laser irradiation, the irradiated surfaces were observed by SEM.

Figure 3 presents the SEM morphologies of the irradiated surfaces under increased scanning speeds, 5 mm s^{-1} (figures 3(a) and (b)) and 10 mm s^{-1} (figures 3(c) and (d)). Other experimental conditions corresponding to figure 3 were the same to those in figure 1. Compared to the results in figures 1 and 2, with increase in the scanning speed, the laser pulse tracks in figure 3 become much clearer with increased width, but the cross-shaped protrusions are not observed. This resulted from the decreased overlap width along a scanning line for the increased scanning speeds, 80 and 75 μm for 5 mm s^{-1} and 10 mm s^{-1} respectively, while it is 84 μm for 1 mm s^{-1}. Thus, for increased scanning speeds, the distance between two laser pulse tracks was increased but heat accumulation along a scanning line was reduced. Corresponding to 5 mm s^{-1} and 10 mm s^{-1} laser scanning, the less heat accumulation led to lower temperature rise compared to that for 1 mm s^{-1} during a single laser shot, and thus few MG materials were vaporized and heated for increased scanning speeds. While, during laser pulse off, the increased distance between

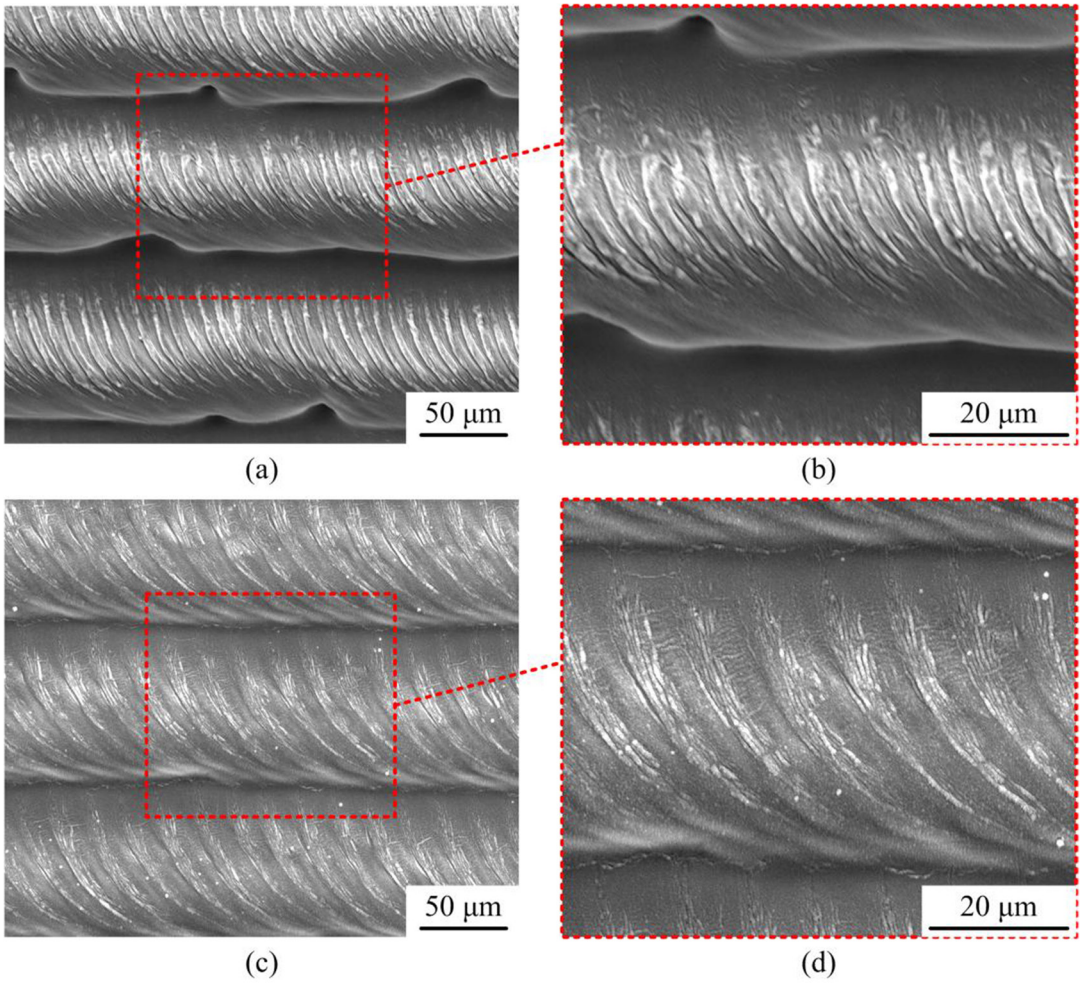

Figure 3. SEM morphologies of the irradiated MG surfaces under increased scanning speeds: (a) and (b) 5 mm s^{-1}, and (c) and (d) 10 mm s^{-1}. Other experimental conditions were the same to those in figure 1, i.e. peak laser power intensity of 1.3×10^{12} W m^{-2} and pulse overlap rate r of 47%.

two laser shots further accelerated the temperature decrease and re-solidification process. These two aspects reduced the formation of ZrN, agreeing well with the XRD results in our previous research that increased scanning speeds suppressed the ZrN peaks [24]. Thus, the formation of radial cracks and line cracks was suppressed. As discussed in section 3.2, the formation of cross-shaped protrusions is related to the line cracks, and hence, cross-shaped protrusions were also suppressed for laser scanning speeds of 5 mm s^{-1} and 10 mm s^{-1}.

Figure 4 presents the SEM morphologies of the irradiated surfaces under increased peak laser power intensities, 3.4×10^{12} W m^{-2} (figures 4(a) and (b)) and 5.3×10^{12} W m^{-2} (figures 4(c) and (d)). Other experimental conditions corresponding to figure 4 were the same to those in figure 1. In figure 4, the irradiated surfaces become irregular and it is difficult to distinguish the micro grooves and laser pulse tracks. However, cross-shaped protrusions had been formed on wrinkled surfaces as shown in figures 4(b) and (d). Furthermore, the cross-shaped protrusions in figure 4 show a larger width compared to that in figure 2(b). With increase in the peak laser power intensity, more MG materials were vaporized and heated, and the recoil pressure generated by vaporization was also increased. Thus, more materials were pushed to flow outward, resulting in wrinkled surfaces during re-solidification. Meanwhile, more vaporized materials could be re-deposited on the irradiated surface, contributing to the increased width of the cross-shaped protrusions as well as micro-sphere-like microstructures in figure 4. Our previous research [24] indicated that the increased peak laser power intensity slightly enhanced the formation of ZrN, and thus further slightly enhanced the formation of cracks during a single laser shot. As the formation of cross-shaped protrusions is related to line cracks, the enhanced cracks could also contribute to the increase in width of the cross-shaped protrusions.

Figure 5 presents the SEM morphologies of the irradiated surfaces under various pulse overlap rates r, 82% (figures 5(a)–(c)), 65% (figure 5(d)), 47% (figure 5(e)), and 29% (figure 5(f)). Other experimental conditions corresponding to figure 5 were the same to those in figure 1. Figure 6 illustrates the comparative results of XRD patterns obtained on the as-cast and irradiated MG surfaces under various pulse overlap rates r. Figure 7 shows the SEM morphologies of the cross-sections before and after acid corrosion under the pulse overlap rates r of 82% (figures 7(a) and (b)) and 47% (figures 7(c) and (d)).

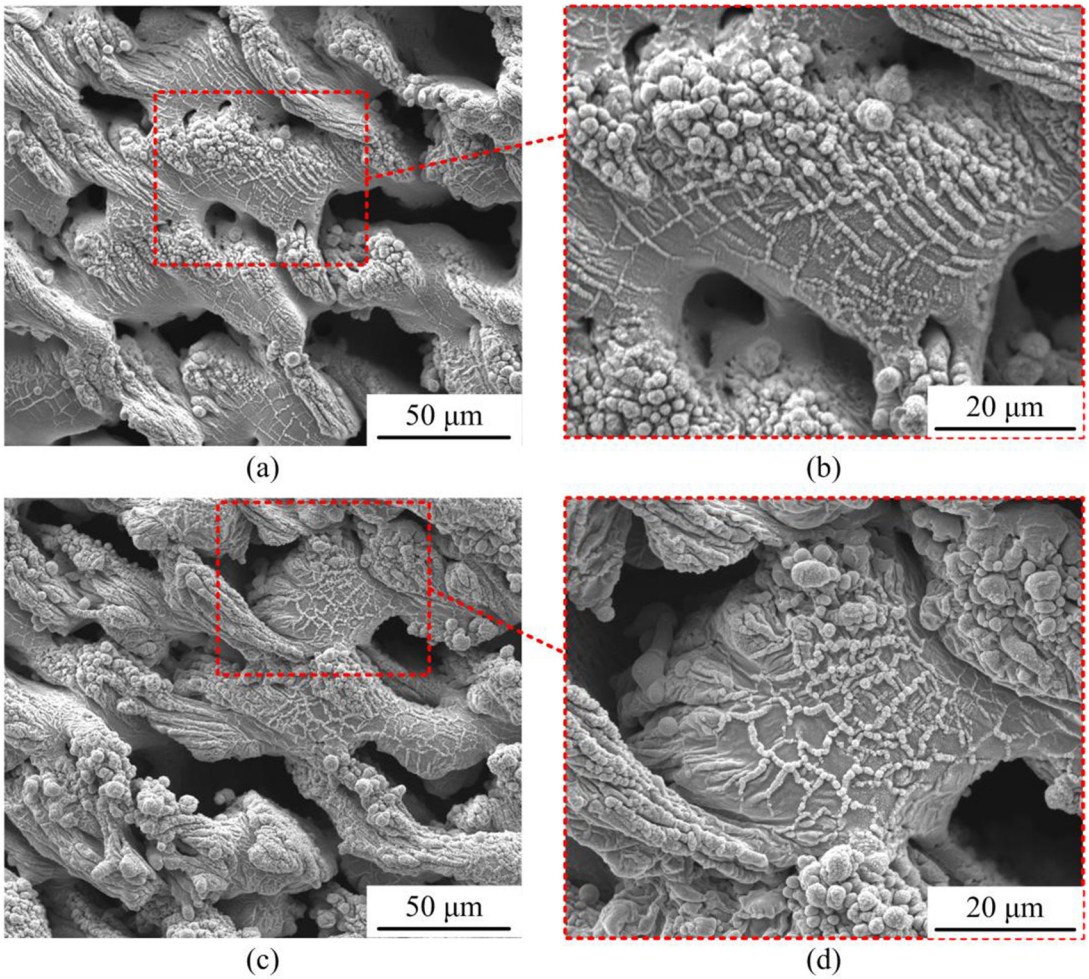

Figure 4. SEM morphologies of the irradiated MG surfaces under increased peak laser power intensities: (a) and (b) 3.4×10^{12} W m^{-2}, and (c) and (d) 5.3×10^{12} W m^{-2}. Other experimental conditions were the same to those in figure 1, i.e. scanning speed of 1 mm s^{-1} and pulse overlap rate r of 47%.

In figures 5(a)–(c), with a large pulse overlap rate r of 82%, the whole irradiated surface was almost covered by the cross-shaped protrusions, which were separated by a narrow laser interactive region. Furthermore, the cross-shaped protrusions as well as surrounding surfaces were covered by nanoparticles, similarly to that shown in figure 2(c). With decrease in the pulse overlap rate r from 82% to 29%, the position of cross-shaped protrusions moved from the side of micro grooves being close to preceding scanning lines to another side being close to the next scanning lines. Results in figure 5 indicate that by controlling the pulse overlap rate r, the cross-shaped protrusions can be tuned to form at various positions of a single scanning line.

In figure 6, the ZrN peaks were slightly weakened with decrease in r from 82% to 29%, implying less formation of ZrN when the pulse overlap rate r decreased. With decrease in r, fewer scanning lines were experienced for the same irradiated region, resulting in less irradiation time and heat accumulation. Thus, fewer MG materials were vaporized and fewer MG materials reacted with the nitrogen gas to form the ZrN.

Furthermore, by comparing the SEM morphologies in figures 5(a) and (d)–(f) which were obtained at the same magnification, it is noted that with decrease in r, the size of the cross-shaped protrusions also decreases. This could be ascribed to the following three reasons. Firstly, less ZrN was generated with decrease in r as shown in figure 6, possibly resulting in small line cracks. Secondly, fewer MG materials were vaporized and re-deposited because of the less irradiation time and heat accumulation with decrease in r. Thirdly, with a decreased r, for example $r = 29\%$, re-deposition of vaporized fine particles may occur only in the very adjacent laser scanning line, while it may occur in the subsequent several laser scanning lines for a large r, for example $r = 82\%$.

In figure 7(a), for $r = 82\%$, some dark regions appear and these regions can also be observed after acid corrosion in figure 7(b). The distance between adjacent dark regions is about 15 μm, agreeing well with the corresponding distance for $r = 82\%$. This indicates that these dark regions were formed in the interface between two adjacent laser shots. As the formation of ZrN is a result of the reaction of the MG materials with the nitrogen gas, ZrN might mainly exist in the top layer of the region irradiated by a single laser shot. The top layer embedded with ZrN was subsequently covered by material flow in adjacent laser shots. For $r = 82\%$, more ZrN was formed as shown in figure 6 and also the pulse overlap width was large. Thus, the microstructures of materials in the interface were significantly

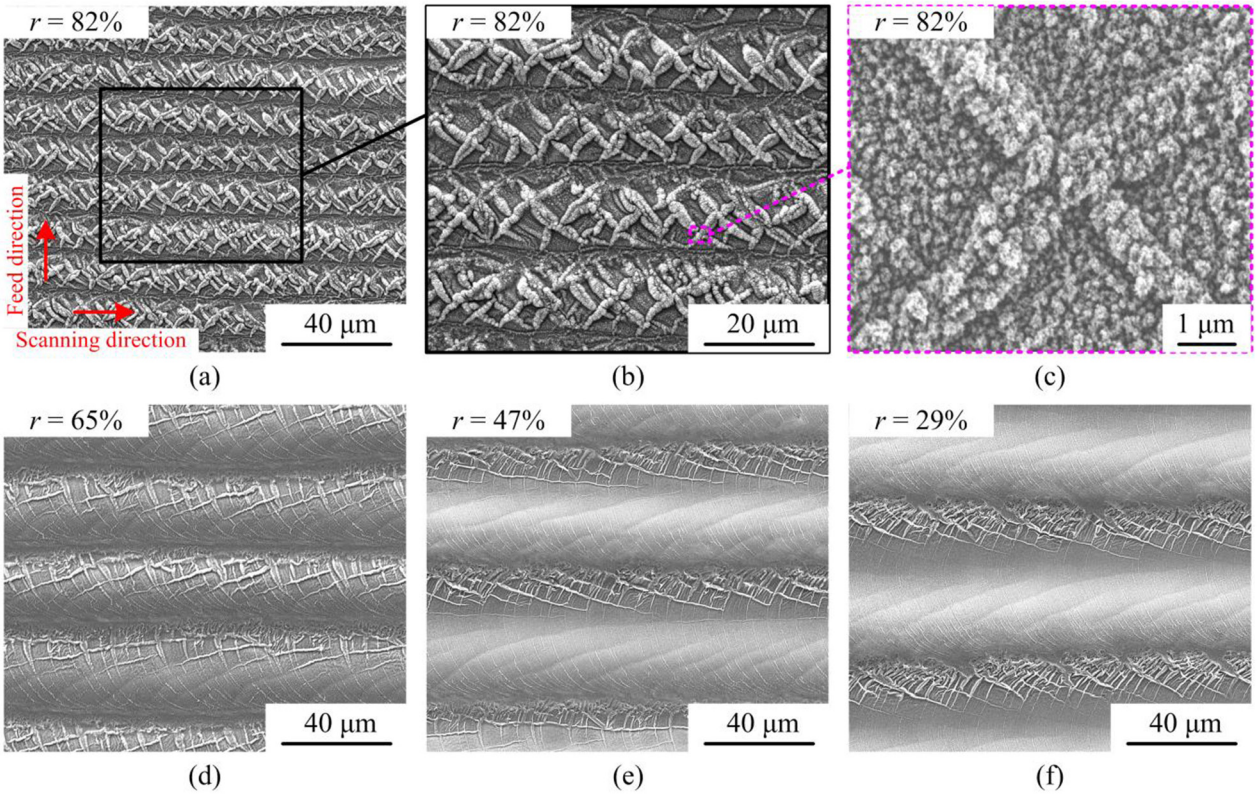

Figure 5. SEM morphologies of the irradiated MG surfaces under different pulse overlap rates: (a)–(c) $r = 82\%$, (d) $r = 65\%$, (e) $r = 47\%$, and (f) $r = 29\%$. Other experimental conditions were the same to those in figure 1, i.e. scanning speed of 1 mm s^{-1} and peak laser power intensity of 1.3×10^{12} W m^{-2}.

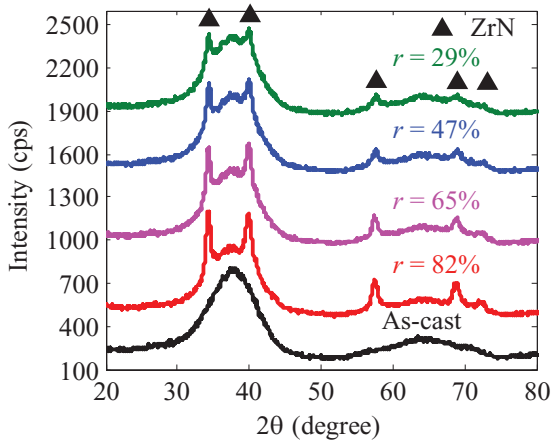

Figure 6. XRD patterns of the as-cast and irradiated MG surfaces under various pulse overlap rates r.

affected, exhibiting different contrast compared with that of the surrounding regions as shown in figures 7(a) and (b). While for $r = 47\%$, no such dark region is clearly visible in figures 7(c) and (d) because of the less formation of ZrN as well as the decreased pulse overlap width. By measuring the depth of the dark regions in figures 7(a) and (b), the affecting depth of MG by laser irradiation under $r = 82\%$ is roughly estimated to be about 8 μm, which is slightly larger than the height of surface patterns. Although laser irradiation affected the microstructures of MG materials in the interface between adjacent laser shots, there is no remarkable difference for the cross-sections before and after acid corrosion as shown in figure 7, indicating that the affecting regions induced by nanosecond pulsed laser irradiation keep good corrosion resistance comparable with original MG. This is due to the fact that the affecting regions still remain the amorphous matrix (broad humps in figure 6) with ZrN embedded. As the emphasis of this study is on the surface patterning, the detailed microstructures of materials in the affecting region as well as their effects on the mechanical properties of MG will be further investigated in the future.

3.4. Formation mechanism of the cross-shaped protrusions

For better tuning the micro-/nano-structures by laser irradiation, understanding the formation mechanisms of the hierarchical surface structures is the premise. Formation mechanisms of micro grooves, laser pulse tracks and nanoparticles have been widely investigated and are well known [20, 21, 23]. Micro grooves are formed by recoil pressure induced outward flow of MG materials and subsequent re-solidification [21]. Laser pulse tracks are generated during the interaction when the subsequent laser shot overlaps the previous laser shot [23]. Nanoparticles are formed by re-deposition of vaporized fine particles [20, 23]. As the cross-shaped protrusions are reported for the first time, their formation mechanism will be given more attention in this study.

As shown in figures 2 and 5, the cross-shaped protrusions were formed at the positions where the line cracks and laser pulse tracks were located. Furthermore, when no line cracks

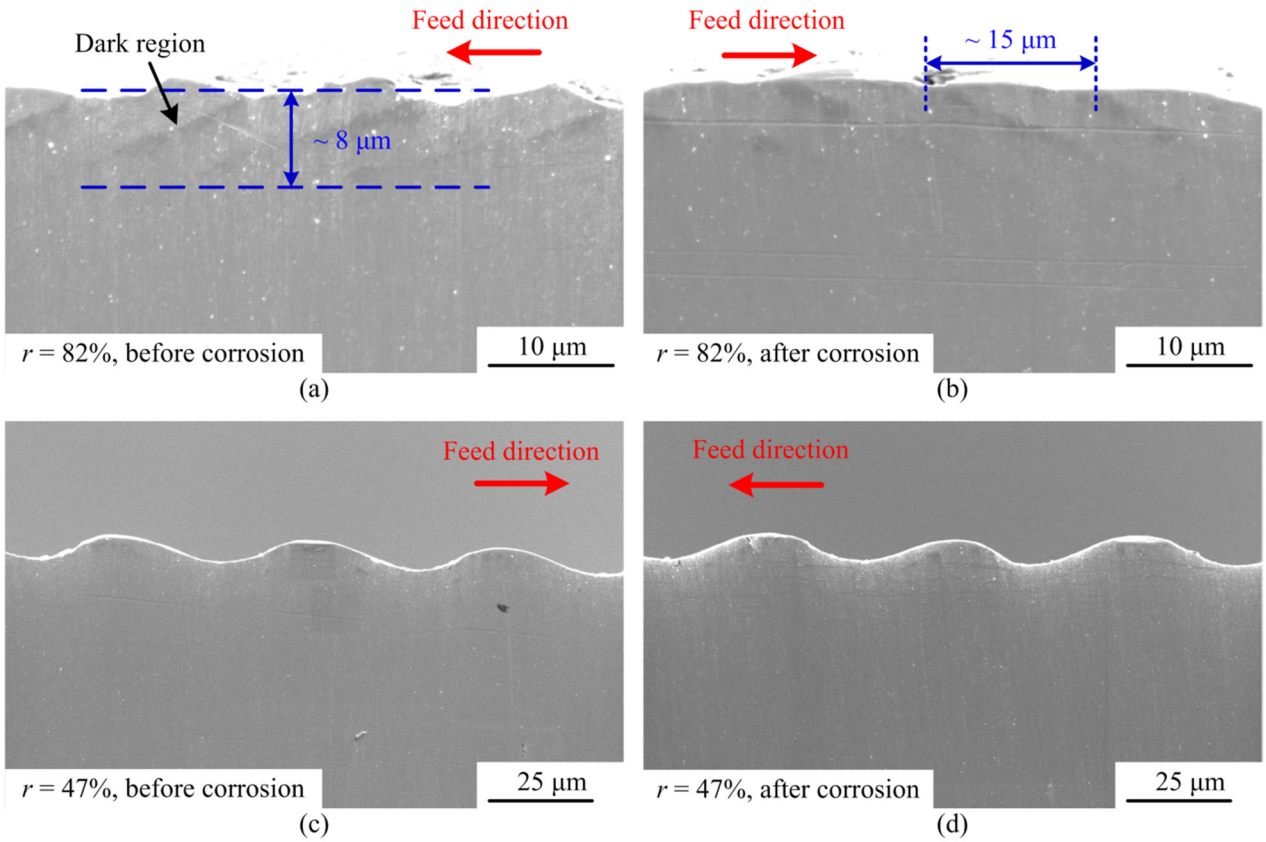

Figure 7. SEM morphologies of the cross-sections before and after acid corrosion under the pulse overlap rates r of 82% ((a) and (b)) and 47% ((c) and (d)).

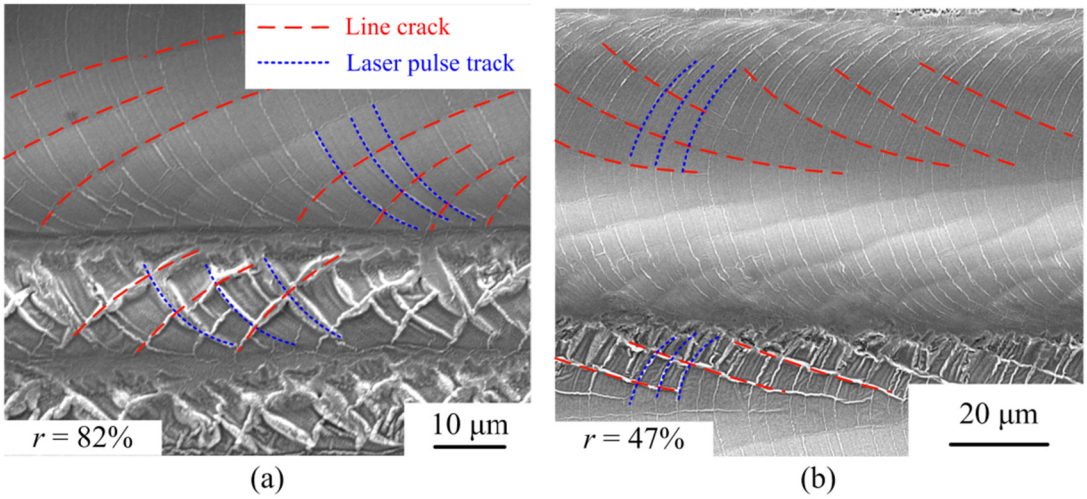

Figure 8. (a) SEM morphology at the last three scanning lines with $r = 82\%$ and (b) SEM morphology at the last two scanning lines with $r = 47\%$.

were generated as shown in figure 3, the cross-shaped protrusions were also not formed. These facts indicate that the formation of line cracks is necessary for the subsequent formation of cross-shaped protrusions. To further clarify the relationship between the cross-shaped protrusions, line cracks, and laser pulse tracks, surface morphologies and characteristics of the laser irradiated regions were further explored by SEM, AFM, and EDX. Figures 8(a) and (b) show the SEM morphologies near the last laser scanning line corresponding to the pulse overlap rates r of 82% and 47%, respectively. As shown in figure 8, line cracks are interlaced with the laser pulse tracks. Interestingly, the line cracks are approximately parallel to one part of the cross-shaped protrusions, while the laser pulse tracks are parallel to another part of the cross-shaped protrusions, independent of the position of cross-shaped protrusions. This further confirms that the cross-shaped protrusions were originated from both the line cracks and laser pulse tracks.

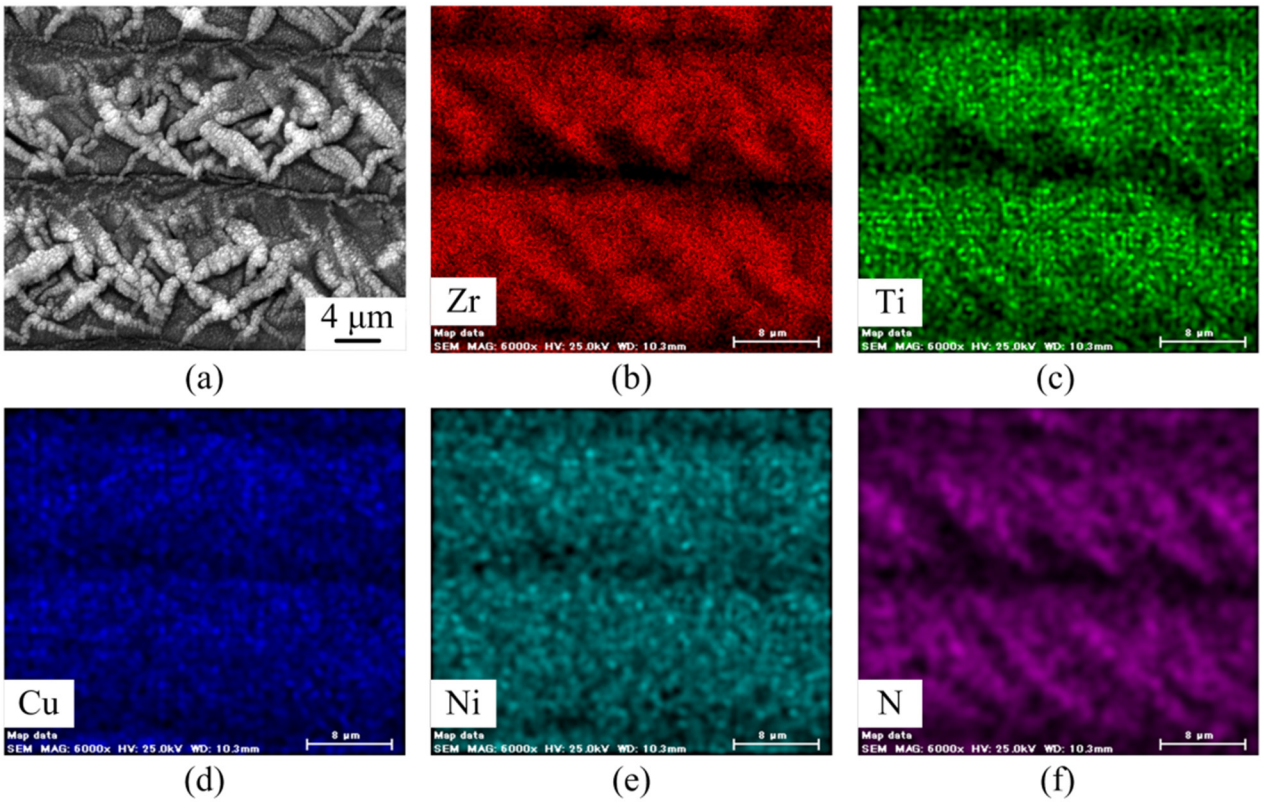

Figure 9. EDX element mappings: (a) mapping region, (b) Zr, (c) Ti, (d) Cu, (e) Ni, and (f) N.

Figures 9(b)–(f) present the element distribution of Zr, Ti, Cu, Ni, and N measured by EDX mapping of the irradiated surface as shown in the SEM morphology in figure 9(a). As Be element is a light chemical element, it was not detected by the EDX system. It can be seen that Ti, Cu, and Ni elements are uniformly distributed on the irradiated surface, while more Zr and N elements are concentrated around the cross-shaped protrusions. Furthermore, the distribution of N element matches well with that of Zr element, suggesting that more ZrN was generated around the cross-shaped protrusions.

Figure 10(a) presents the AFM morphology around a line crack, which was obtained on the last laser scanning line shown in figure 8(a). Figure 10(b) illustrates the profile of the dotted line in figure 10(a), where the line crack shows concave surface with a maximum depth of ~70 nm and a width of ~6 μm. The AFM morphology further confirms that the radial open cracks formed during a single laser shot had evolved to be closed cracks during subsequent laser irradiation along a scanning line. Figure 10(c) presents the 3D morphology around a cross-shaped protrusion obtained on the penultimate laser scanning line shown in figure 8(a), and figure 10(d) illustrates the profile of the dotted line in figure 10(c). It is noted that the cross-shaped protrusion has a height of hundreds of nanometers and it is covered by nanoparticles, agreeing well with the SEM results in figures 5(a)–(c).

Compared to the slightly concave line cracks as well as very small and narrow laser pulse tracks in the last laser scanning line as shown figures 8(a) and 10(a), the cross-shaped protrusions in figures 5(a)–(c), 8(a) and 10(c) are convex with a height of hundreds of nanometers, suggesting that MG materials were selectively extruded from both the line cracks and laser pulse tracks during the subsequent laser scanning lines. This scenario is reasonable in consideration of enhanced laser energy absorption [26, 28, 29] and higher localized thermal resistivity [25, 27, 28] at positions of the line cracks and laser pulse tracks, compared to surrounding irradiated surfaces. Previous research indicated that the enhanced absorption of laser energy by cracks possibly resulted from the following reasons. Firstly, multiple times of laser reflection inside cracks increase the laser absorption and heating efficiency [28]. Secondly, particulate matter may be trapped in cracks, which could work as absorbing center for laser energy [29]. Thirdly, cracks lead to local enhancement of the electric field strength in laser beam [26]. Meanwhile, cracks perturb the heat flow, resulting in high localized thermal resistivity [25]. Similar situations may also occur in laser pulse tracks because they have similar features to cracks.

Accordingly, taking line cracks for example, figure 11 illustrates the possible formation mechanism of cross-shaped protrusions. In figure 11(a), micro grooves and pileups with line cracks on their surface as shown in figures 1(b)–(d) were generated on the MG surface along a laser scanning line after nanosecond pulsed laser irradiation in nitrogen gas using a Gauss beam with a peak laser power intensity I_0 and a laser beam radius R defined by I_0/e^2. Over the beam radius R, MG surface may be only heated as HAZ as shown in figure 1(b) because of relatively low laser power intensity. After one line scanning, laser beam was shifted with a given pulse overlap rate r, for example $r = 29\%$ shown in figure 11(b), and then continued scanning along a line. As shown in figure 11(b),

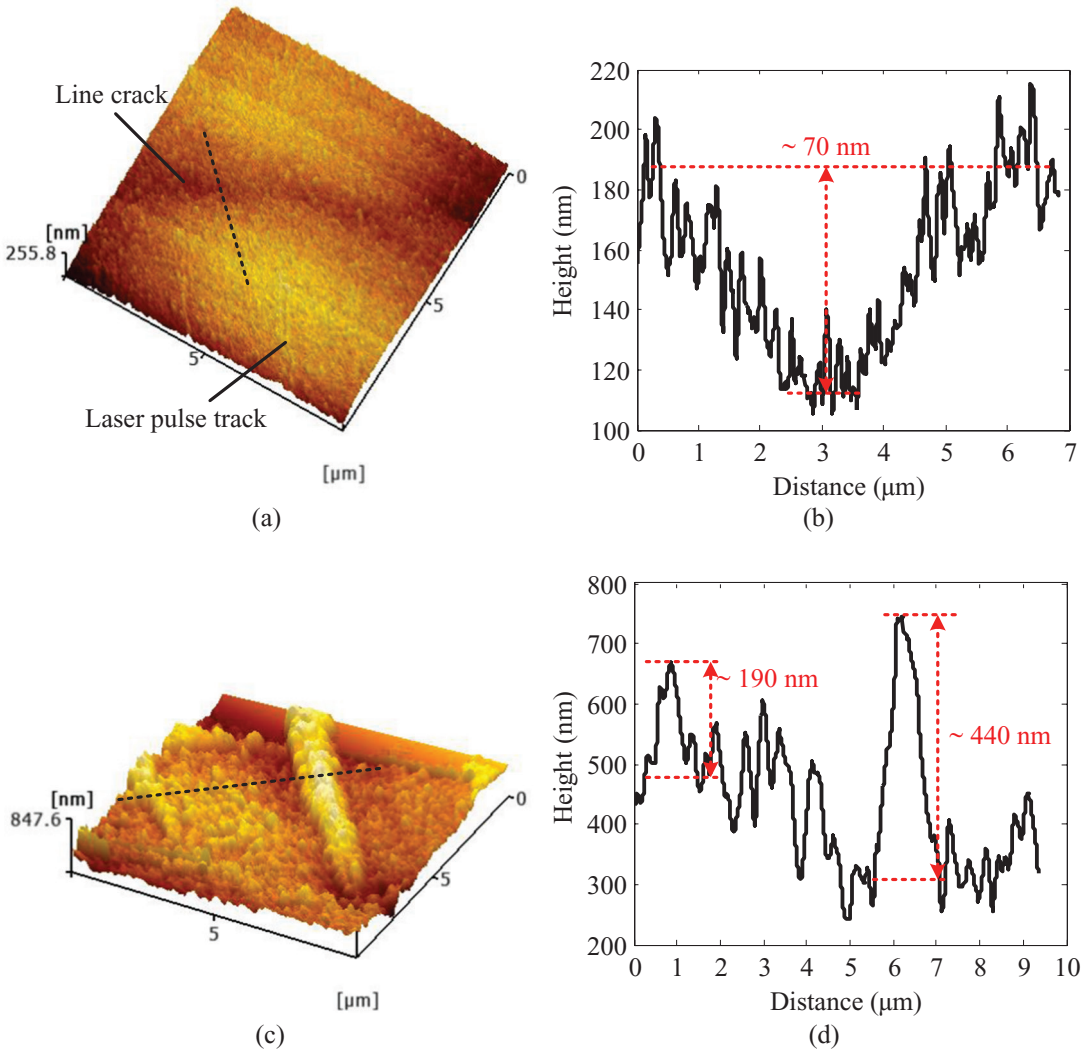

Figure 10. (a) AFM morphology around a line crack obtained on the last scanning line shown in figure 8(a), (b) profile of the dotted line in (a), (c) AFM morphology around a cross-shaped protrusion obtained on the penultimate laser scanning line shown in figure 8(a), (d) profile of the dotted line in (c).

some line cracks formed by the preceding laser scanning line were still in the irradiation range of Gauss laser beam. In consideration of their enhanced laser energy absorption and high localized thermal resistivity, the line cracks being very close to the overlap region as shown in figure 11(b) could be affected by the laser beam over the beam radius R. Figure 11(c) presents the local enlarged view of figure 11(b), illustrating the possible laser-MG interaction around a line crack being close to the overlap region during laser on and off. When laser was on, the line crack as well as surrounding surface was heated, and meanwhile, thermal expansion induced thermal stress was generated inside the heated region. Because of high laser energy absorption and localized thermal resistivity, the local temperature at a crack increased fast and it could be over the glass transition point. While, because of low laser power intensity over the beam radius R, the surrounding surface was only heated and the temperature was still below the glass transition point. It is well known that MGs over the glass transition temperature have superplasticity, which is the foundation for widely used thermoplastic forming of MGs [3, 6, 14, 30, 31, 34–36]. Thus, with the role of thermal stress, some MG materials were selectively extruded from the line cracks as shown in figure 11(c). Additionally, the recoil pressure generated by material vaporization in adjacent laser scanning lines resulted in the overall deformation of MG materials in the overlap region towards the direction of preceding scanning lines, and this may also contribute to the extrusion of MG materials from the line cracks. Similar processes could also occur at the position of laser pulse tracks. The extruded MG materials from the line cracks and laser pulse tracks interlaced with each other, forming the embryo of the cross-shaped protrusions. During laser off, vaporized fine particles were readily re-deposited on the surface of cross-shaped protrusions because of their increased surface area, and thus, the cross-shaped protrusions further grew up with nanoparticles covered. This is well confirmed by the fact that more Zr and N elements are distributed around the cross-shaped protrusions as shown in figure 9. By tuning the pulse overlap rate r, MG materials can be controlled to be extruded from the line cracks and laser pulse tracks at various

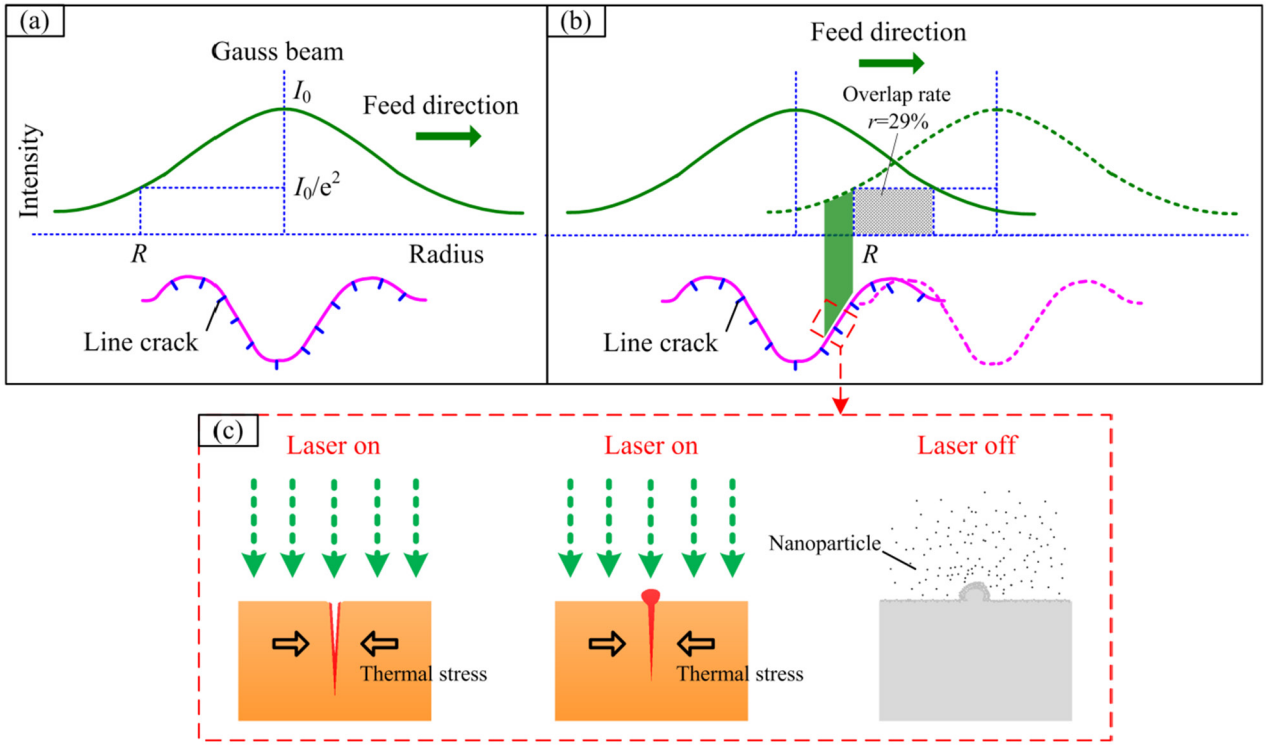

Figure 11. Schematic diagrams illustrating the formation mechanism of cross-shaped protrusions. (a) Formation of line cracks after single line scanning, (b) interaction of two scanning line with a pulse overlap rate r of 29%, and (c) local enlarged view in figure 11(b) showing the laser-MG interaction around a line crack during laser on and off.

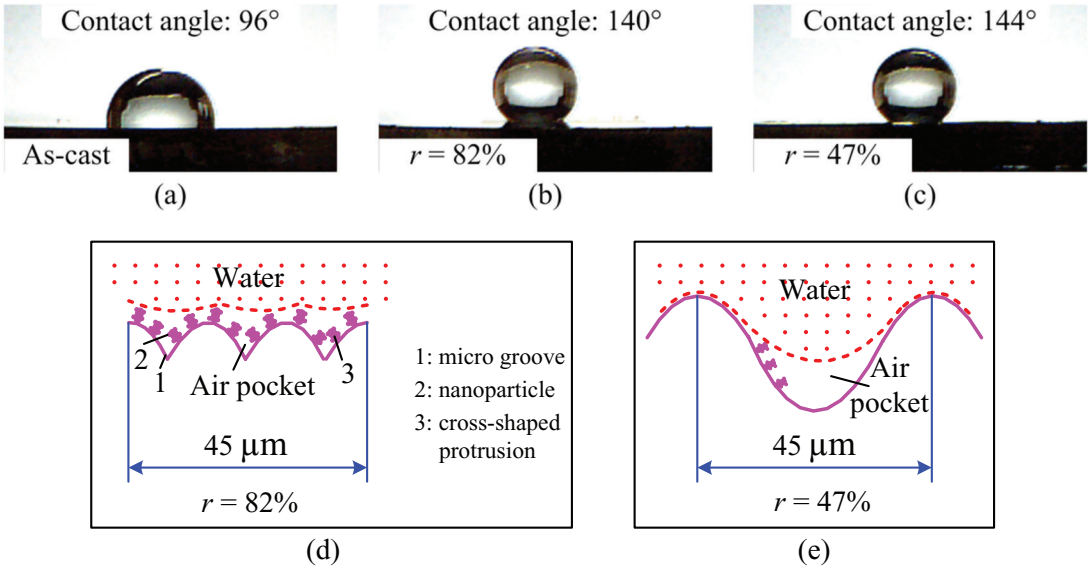

Figure 12. Contact angle of as-cast (a) and laser patterned MG surface with $r = 82\%$ (b) and 47% (c). (d) and (e) Local contact statuses between the water droplet and the laser patterned surfaces corresponding to $r = 82\%$ and 47%, respectively.

positions of a single scanning line, and thus the cross-shaped protrusions were generated at various positions as shown in the comparative results in figures 5 and 8.

3.5. Effects of surface structures on hydrophobicity

It is commonly reported that the structured surface can effectively enhance its hydrophobicity [10, 11, 14]. To study the effects of laser patterned surface structures on hydrophobicity, figures 12(a)–(c) show the comparative results of water contact angle between the as-cast and laser patterned MG surfaces. The featureless smooth surface of the as-cast MG after grinding and polishing only induces a contact angle of 96° in figure 12(a). While, with the hierarchical surface structures as shown in figures 5(a)–(c) formed by laser irradiation with $r = 82\%$, the contact angle remarkably increases to be 140° in

figure 12(b). Furthermore, with a decreased pulse overlap rate r of 47%, the contact angle also remarkably increases to be 144°. As shown in figures 5(a) and (e), the surface morphologies for $r = 82\%$ and 47% are hugely different. For the case of $r = 47\%$, deeper and wider micro grooves with fewer cross-shaped protrusions were generated as shown in figure 5(e) because of large distance between two adjacent scanning lines. While, for $r = 82\%$, the micro grooves are shallow and narrow as shown in figures 5(a) and (b) because of the small distance between two adjacent scanning lines. This difference in surface structure may suggest different mechanisms resulting in increase in contact angle under various pulse overlap rates r. It is well known that a composite of solid–liquid–air interface will be formed when the water droplet contacts with a heterogeneous surface [9, 10]. According to the modified Cassie–Baxter model [37], the contact angle θ_{CB} on a structured surface and the contact angle θ_C on a smooth surface with identical chemical composition satisfy the following equation:

$$\cos\theta_{CB} = f_{s-l}(\cos\theta_C + 1) - 1 \quad (1)$$

where f_{s-l} is the area fraction of the solid–liquid interface and θ_C here is 96° according to figure 12(a). As the contact angle for $r = 82\%$ and 47% is almost the same, it means that almost the same area fraction of the solid–liquid interface, i.e. almost the same area fraction of the air–liquid interface, was generated under these two cases although their surface structures are hugely different. According to the residual morphologies in figures 5(a) and (e), figures 12(d) and (e) illustrate the possible local contact statuses between the water droplet and the structured surfaces corresponding to $r = 82\%$ and 47%, respectively. For $r = 47\%$, the micro grooves on the irradiated surface are relatively deep and wide, and the surface of micro grooves are relatively smooth with fewer cross-shaped protrusions. Thus, a large amount of air could be trapped in the micro grooves as shown in figure 12(e), resulting in large area fraction of the air–liquid interface. In this case, micro grooves may play a dominant role in increasing of the contact angle. While, for $r = 82\%$, a large amount of air could be trapped in hierarchical surface structures forming the air–liquid interface as shown in figure 12(d), especially the uniformly distributed cross-shaped protrusions covered by nanoparticles because of their large effective surface area [10]. Furthermore, corresponding to the same length of 45 μm, the amount of the repeated surface structures for $r = 82\%$ is three times of that for $r = 47\%$. Thus, although the micro grooves are relatively shallow and narrow, a large area fraction of the air–liquid interface could also be generated, increasing the contact angle. Although the dominant reason leading to the increase in contact angle for various pulse overlap rates r may be different, the comparative results in figure 12 indicate that the patterned MG surface by nanosecond pulsed laser irradiation in nitrogen gas can efficiently increase the water contact angle, i.e. the hydrophobicity, which will enrich the functional applications of MG as structural and engineering materials.

4. Conclusions

Nanosecond pulsed laser irradiations were performed under various laser scanning speeds, power intensities, and pulse overlap rates in nitrogen gas for patterning Zr-based MG surface. Microstructures formed on the irradiated surfaces were compared and their formation mechanisms were discussed. The main findings include:

1. Three kinds of surface structures, i.e. micro grooves, submicron cross-shaped protrusions, and nanoparticles, were generated at a low laser scanning speed (1 mm s^{-1}). This kind of hierarchical surface structure formation was repeatable under various laser power intensities and pulse overlap rates.
2. At higher laser scanning speeds (5 and 10 mm s^{-1}), cross-shaped protrusions were not formed. This might be due to that no line cracks were generated at these scanning speeds.
3. By changing the pulse overlap rate, the distribution of the hierarchical surface structures could be tuned. With decrease in the pulse overlap rate, the ZrN formation was suppressed, and the size of the cross-shaped protrusions decreased.
4. The cross-shaped protrusions were formed along the line cracks and the laser pulse tracks, respectively. Due to the enhanced laser absorption and localized thermal resistivity at cracks and laser pulse tracks, the MG material was selectively extruded from these surface defects, forming the cross-shaped protrusions.
5. EDX mapping results showed uniform distribution of Ti, Cu, and Ni elements, and more concentrated distribution of Zr and N elements around the cross-shaped protrusions.
6. The patterned Zr-based MG surfaces showed remarkably enhanced hydrophobicity compared to the as-cast MG surface.

Acknowledgments

This work was supported by Grant-in-Aid for JSPS Fellows (Grant No. 26-04048). The authors thank Jun Noguchi at Keio University for technical support during the laser irradiation experiments.

References

[1] Trexler M M and Thadhani N N 2010 Mechanical properties of bulk metallic glasses *Prog. Mater. Sci.* **55** 759–839
[2] Wang W H 2012 The elastic properties, elastic models and elastic perspectives of metallic glasses *Prog. Mater. Sci.* **57** 487–656
[3] Kumar G, Tang H X and Schroers J 2009 Nanomoulding with amorphous metals *Nature* **457** 868–72
[4] Huang H, Zhang J L, Shek C H and Yan J W 2016 Effects of pre-compression deformation on nanoindentation response

of $Zr_{65}Cu_{15}Al_{10}Ni_{10}$ bulk metallic glass *J. Alloys Compd.* **674** 223–8
[5] Su C, Chen Y, Yu P, Song M, Chen W and Guo S F 2016 Linking the thermal characteristics and mechanical properties of Fe-based bulk metallic glasses *J. Alloys Compd.* **663** 867–71
[6] Plummer J and Johnson W L 2015 Is metallic glass poised to come of age? *Nat. Mater.* **14** 553–5
[7] Li F C, Song M, Ni S, Guo S F and Liao X Z 2016 Correlation between hardness and shear banding of metallic glasses under nanoindentation *Mater. Sci. Eng.* A **657** 38–42
[8] Chen N *et al* 2013 A novel Ti-based nanoglass composite with submicron-nanometer-sized hierarchical structures to modulate osteoblast behaviors *J. Mater. Chem.* B **1** 2568–74
[9] He Y X, Peng Y, Li Z, Ma J, Zhang X Y, Liu K S, Wang W H and Jiang L 2016 Bio-inspired multifunctional metallic glass *Sci. China Chem.* **59** 271–6
[10] Li N, Xia T, Heng L P and Liu L 2013 Superhydrophobic Zr-based metallic glass surface with high adhesive force *Appl. Phys. Lett.* **102** 251603
[11] Ma J, Zhang X Y, Wang D P, Zhao D Q, Ding D W, Liu K and Wang W H 2014 Superhydrophobic metallic glass surface with superior mechanical stability and corrosion resistance *Appl. Phys. Lett.* **104** 173701
[12] Chen N *et al* 2011 Formation and properties of Au-based nanograined metallic glasses *Acta Mater.* **59** 6433–40
[13] Ketov S V *et al* 2015 Nanostructured Zr-Pd metallic glass thin film for biochemical applications *Sci. Rep.* **5** 7799
[14] Xia T, Li N, Wu Y and Liu L 2012 Patterned superhydrophobic surface based on Pd-based metallic glass *Appl. Phys. Lett.* **101** 081601
[15] Liu K S, Li Z, Wang W H and Jiang L 2011 Facile creation of bio-inspired superhydrophobic Ce-based metallic glass surfaces *Appl. Phys. Lett.* **99** 261905
[16] Zhao K, Liu K S, Li J F, Wang W H and Jiang L 2009 Superamphiphobic CaLi-based bulk metallic glasses *Scr. Mater.* **60** 225–7
[17] Gleiter H 2013 Nanoglasses: a new kind of noncrystalline materials *Beilstein J. Nanotechnol.* **4** 517–33
[18] Gleiter H, Schimmel T and Hahn H 2014 Nanostructured solids—from nano-glasses to quantum transistors *Nano Today* **9** 17–68
[19] Liu Y, Jiang M Q, Yang G W, Guan Y J and Dai L H 2011 Surface rippling on bulk metallic glass under nanosecond pulse laser ablation *Appl. Phys. Lett.* **99** 191902
[20] Jiang M Q, Wei Y P, Wilde G and Dai L H 2015 Explosive boiling of a metallic glass superheated by nanosecond pulse laser ablation *Appl. Phys. Lett.* **106** 021904
[21] Williams E and Brousseau E B 2016 Nanosecond laser processing of $Zr_{41.2}Ti_{13.8}Cu_{12.5}Ni_{10}Be_{22.5}$ with single pulses *J. Mater. Process. Technol.* **232** 34–42
[22] Zhu Y H, Fu J, Zheng C and Ji Z 2016 Effect of nanosecond pulse laser ablation on the surface morphology of Zr-based metallic glass *Opt. Laser Technol.* **83** 21–7
[23] Huang H, Jun N, Jiang M Q, Ryoko M and Yan J W 2016 Nanosecond pulsed laser irradiation induced hierarchical micro/nanostructures on Zr-based metallic glass substrate *Mater. Des.* **109** 153–61
[24] Huang H, Noguchi J and Yan J W 2016 Shield gas induced cracks during nanosecond-pulsed laser irradiation of Zr-based metallic glass *Appl. Phys.* A **122** 881
[25] Li T, Almond D P and Rees D A S 2011 Crack imaging by scanning pulsed laser spot thermography *Ndt&E Int.* **44** 216–25
[26] Bloembergen N 1973 Role of cracks, pores, and absorbing inclusions on laser-induced damage threshold at surfaces of transparent dielectrics *Appl. Opt.* **12** 661–4
[27] Schlichting J, Ziegler M, Maierhofer C and Kreutzbruck M 2012 Flying laser spot thermography for the fast detection of surface breaking cracks *18th World Conf. on Nondestructive Testing (16–20 April 2012*, *Durban, South Africa)*
[28] Myrach P, Polomski B, Le claire E, Unnikrishnakurup S, Vengara N, Balasubramaniam K and Ziegler M 2016 Thermographic crack detection in hot steel surfaces *19th World Conf. on Non-Destructive Testing* (*13–17 June 2016*, *Munich, Germany)*
[29] Feit M D and Rubenchik A M 2003 Influence of subsurface cracks on laser induced surface damage *SPIE Boulder Damage Symp. XXXV Annual Symp. on Optical Materials for High Power Lasers (22–24 September 2003*, *Boulder, CO)*
[30] Li N, Chen W and Liu L 2016 Thermoplastic micro-forming of bulk metallic glasses: a review *Jom-Us* **68** 1246–61
[31] Schroers J 2010 Processing of bulk metallic glass *Adv. Mater.* **22** 1566–97
[32] Huang H and Yan J W 2015 On the surface characteristics of a Zr-based bulk metallic glass processed by microelectrical discharge machining *Appl. Surf. Sci.* **355** 1306–15
[33] Semak V and Matsunawa A 1997 The role of recoil pressure in energy balance during laser materials processing *J. Phys. D: Appl. Phys.* **30** 2541–52
[34] Hu Z, Gorumlu S, Aksak B and Kumar G 2015 Patterning of metallic glasses using polymer templates *Scr. Mater.* **108** 15–8
[35] Hasan M, Schroers J and Kumar G 2015 Functionalization of metallic glasses through hierarchical patterning *Nano Lett.* **15** 963–8
[36] Sarac B, Ketkaew J, Popnoe D O and Schroers J 2012 Honeycomb structures of bulk metallic glasses *Adv. Funct. Mater.* **22** 3161–9
[37] Cassie A B D and Baxter S 1944 Wettability of porous surfaces *Trans. Faraday Soc.* **40** 546–51